

Exploring shock-capturing schemes for Particles on Demand simulation of compressible flows

Ehsan Reyhanian^a, Benedikt Dorschner^a, Ilya Karlin^a

^a*Department of Mechanical and Process Engineering, ETH
Zurich, 8092, Zurich, Switzerland*

Abstract

In this exploratory study, we apply shock-capturing schemes within the framework of the Particles on Demand kinetic model to simulate compressible flows with mild and strong shock waves and discontinuities. The model is based on the semi-Lagrangian method where the information propagates along the characteristics while a set of shock-capturing concepts such as the total variation diminishing and weighted essentially non-oscillatory schemes are employed to capture the discontinuities and the shock-waves. The results show that the reconstruction schemes are able to remove the oscillations at the location of the shock waves and together with the Galilean invariance nature of the Particles on Demand model, stable simulations of mild to extreme compressible benchmarks can be carried out. Moreover, the essential numerical properties of the reconstruction schemes such as their spectral analysis and order of accuracy are discussed.

Keywords: Particles on Demand, Shock-capturing schemes, Total variation diminishing, weighted essentially non-oscillatory schemes

1. Introduction

Simulation of compressible high-speed flows have been a long-standing topic of research in computational fluids dynamics (CFD). Various advanced numerical schemes have been developed to resolve small-scale features of shocked flows as well as capturing the discontinuities. As a classical CFD contradiction, while a sufficient amount of dissipation is required for capturing the discontinuities, it can negatively affect resolving small structures [1]. It is crucial for a numerical scheme to maintain high order of accuracy in

smooth parts of the solution while being able to capture discontinuities. To this end, different classes of numerical schemes have been developed such as total variation diminishing (TVD) [2], essentially non-oscillatory (ENO) [3], weighted ENO (WENO) [4] and targeted ENO (TENEO) [5].

The lattice Boltzmann method (LBM) is a modern approach in the field of computational physics, as a recast of fluid dynamics into the kinetic theory of designer particles and has shown a promising performance in various regimes of fluid dynamics ranging from micro [6, 7], multiphase [8, 9, 10, 11] and compressible [12, 13, 14, 15] to complex flows and turbulence [16, 17]. The LB equation describes the evolution of the populations $f_i(\mathbf{x}, t)$ discretized in the velocity space through the discrete particle velocities $\mathbf{c}_i; i = 1, \dots, Q$ with simple rules of streaming and relaxation toward the local equilibrium $f_i^{\text{eq}}(\mathbf{x}, t)$.

Despite the considerable success of LBM in recent decades, there exist inherent restrictions associated with this method. The most important is the violation of the Galilean invariance which limits the application of LBM to low Mach numbers or incompressible flows [18, 19]. However, due to the extensive applications of compressible flows such as flows with strong shocks and discontinuities or compressible multiphase flows, developing a kinetic approach to model these setups is still an open field of research in the LB community.

There have been various attempts to overcome the insufficiencies in LB and enable simulations up to higher Mach numbers. Among those, the recently developed "Particles on Demand for Kinetic Theory" or the so-called "PonD" method is noteworthy, which removes these limitations by defining adaptive sets of microscopic velocities, leading to a Galilean-invariant scheme. The main idea of PonD is to sample particle's velocities based on the local thermodynamics and velocity of the flow, which is significantly different from the conventional Gaussian-Hermit sampling at the core of LBM. This new representation of the kinetics with particles subject to optimal gauges or reference frames leads to error-free equilibrium.

While the PonD kinetic theory holds the underlying essential basis, i.e. Galilean invariance, it still requires to be equipped with proper numerical schemes to handle high-Mach simulations. In particular, due to the off-lattice property of this method, using interpolation is inevitable which potentially

results in oscillatory solutions. This especially concerns setups with strong shocks and discontinuities. These oscillations might trigger negative pressures and temperatures which will blow up the simulations eventually. In this paper, the necessary numerical tools for stable simulations of such flows are developed.

2. Kinetic equations

In PonD, the discrete velocities are defined as

$$\mathbf{v}_i = \sqrt{\theta} \mathbf{c}_i + \mathbf{u}, \quad (1)$$

where $\theta = T/T_L$ for an ideal gas, T is the local temperature, T_L is a constant particular to each lattice known as the lattice temperature [20] and \mathbf{u} is the local flow velocity. Equation (1) describes that the peculiar velocities \mathbf{c}_i are first scaled by some definite factor of the square root of the local temperature and then shifted by the local velocity of the flow. While the former revokes the restriction on the lattice temperature T_L , the latter results in Galilean invariance. The populations corresponding to the reference frame $\lambda = \{T, \mathbf{u}\}$ are denoted by f_i^λ . Similar to LBM, the kinetic equations can split into two main parts; Collision with an exact equilibrium populations

$$f_i^*(\mathbf{x}, t) = f_i(\mathbf{x}, t) + \omega(\rho W_i - f_i)_{(\mathbf{x}, t)}, \quad (2)$$

where $f_i^*(\mathbf{x}, t)$ are the post-collision populations which are computed at the gauge $\lambda = \lambda(\mathbf{x}, t)$, ω is the relaxation parameter related to the viscosity and W_i are conventional LBM lattice weights known for any set of discrete speeds \mathcal{C} . The streaming step shall be implemented via the semi-Lagrangian method where the information at the monitoring point (\mathbf{x}, t) is updated by traveling back through the characteristics to reach the departure point $\mathbf{x}_d(i) = \mathbf{x} - \mathbf{v}_i \delta t$. However, due to the dependency of the discrete velocities (1) on the local flow field, the departure point may be located off the grid points. This is in contrast to LBM, where the lattice provides exact streaming along the links. Hence, the information at the departure point must be interpolated through the neighboring points. Furthermore, in order to be consistent, the populations at the departure point must be in the same reference frame as the monitoring point. Hence, the populations at the collocation points used for the interpolation are first transformed to the gauge of the monitoring

point and then interpolated [14]. Finally, the advection step is formulated as

$$f(\mathbf{x}, t) = \sum_{p=0}^{N-1} \Lambda(\mathbf{x}_d - \mathbf{x}_p) \mathcal{G}_{\lambda_p}^\lambda f^{*\lambda_p}(\mathbf{x}_p, t), \quad (3)$$

where \mathbf{x}_p , $p = 0, \dots, N - 1$ denote the collocation points (grid points) around the departure point and Λ is the interpolation kernel. As mentioned before, the populations are transformed using the transformation Matrix \mathcal{G} . In general, a set of populations at gauge λ can be transformed to another gauge λ' by matching the Q linearly independent moments:

$$\mathbf{M}_{mn}^\lambda = \sum_{i=1}^Q f_i^\lambda v_{ix}^m v_{iy}^n, \quad (4)$$

where m and n are integers. This may be written in the matrix product form as $\mathbf{M}^\lambda = \mathcal{M}_\lambda f^\lambda$ where \mathcal{M} is the $Q \times Q$ linear map. Requiring that the moments must be independent from the choice of the reference frame, leads to the matching condition:

$$\mathcal{M}_{\lambda'} f^{\lambda'} = \mathcal{M}_\lambda f^\lambda, \quad (5)$$

which yields the transformed populations:

$$f^{\lambda'} = \mathcal{G}_\lambda^{\lambda'} f^\lambda = \mathcal{M}_{\lambda'}^{-1} \mathcal{M}_\lambda f^\lambda. \quad (6)$$

Finally, the macroscopic values are evaluated by taking the pertinent moments

$$\rho = \sum_i f_i, \quad (7)$$

$$\rho \mathbf{u} = \sum_i f_i \mathbf{v}_i, \quad (8)$$

$$\rho u^2 + D\rho T = \sum_i f_i v_i^2, \quad (9)$$

The implicitness in the above equations require a predictor-corrector step to find the co-moving reference frame. Hence, the same procedure is repeated

by imposing the new evaluated velocity and temperature until the convergence is achieved. For more details, see [14].

In this paper, the ideal-gas EoS $p = \rho e(\gamma - 1)$ is adopted, where $e = e(T)$ is the specific internal energy and the specific-heat ratio is set to $\gamma = 1.4$ unless stated otherwise. To have an arbitrary value of γ , a second set of populations is employed [21]. However, when using a standard lattice such as $D2Q9$, they are designed to carry the total energy with the equilibrium [22]

$$g_i^{\text{eq}} = \rho W_i (2e - DT + v_i^2), \quad (10)$$

where D is the dimension.

Finally, we comment that the sign u is interchangeably used in this paper as the flow velocity and also the solution function.

3. Reconstruction step

The reconstruction step is one of the most crucial elements in PonD during the advection process. While the transformation part is done merely by the moment-invariance rule, there are various options for the interpolation process. The choice of the reconstruction scheme will strictly affect the solution as well as numerical properties such as conservation and oscillations. In this section, we will explore a wide range of reconstruction schemes, from the basic interpolation methods to non-oscillatory high-resolution schemes and assess their performance in PonD. In order to have a shock-capturing scheme, we make use of the TVD (Total Variation Diminishing) principle, as well as the WENO (Weighted Essentially non-Oscillatory) method.

3.1. Interpolation schemes

Here, we will elaborate the interpolation schemes we have used in this paper. Our experiments show that the choice of the interpolation kernel has significant effects on the accuracy and validity of the results.

We start by considering the one-dimensional semi-Lagrangian advection along the characteristic velocity v during one time step δt . The domain is discretized into Nx points $x_j; j = 0, \dots, Nx - 1$ using equally distant intervals $\delta x = x_j - x_{j-1}$. Without loss of generality, we assume that $v > 0$ and

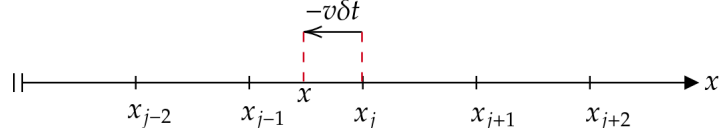


Figure 1: Schematic of the semi-Lagrangian advection in one dimension during the time step δt along the characteristic velocity v .

$x = x_j - v\delta t$ is the interpolating point (see Fig. 1). The fundamental formula for the interpolation reads [23]

$$\tilde{\phi}(x, \delta x) = \sum_{j=-\infty}^{\infty} \phi(x_j) \Lambda(x - x_j, \delta x), \quad (11)$$

where Λ is the interpolation kernel.

3.1.1. Lagrange polynomials

The basic interpolation model is the Lagrange polynomials denoted by $L_N(u)$, where N is the order of interpolation and $u = |x - x_j|/\delta x$. In this paper, we use the 4-point stencil centered around the interpolating point $S = \{x_{j-2}, x_{j-1}, x_j, x_{j+1}\}$. The resulting kernel is a 4th order accurate interpolating kernel:

$$L_4(u) = \begin{cases} -\frac{1}{2}(1 - u^2)(u - 2), & 0 \leq u \leq 1, \\ -\frac{1}{6}(u - 1)(u - 2)(u - 3), & 1 \leq u \leq 2, \\ 0, & \text{otherwise.} \end{cases} \quad (12)$$

In the literature, this is also known as the Everett's formula. [24]

3.1.2. Moment conserving schemes

We assume that the quantity q at a set of points x_p is interpolated through the mesh points x_i . The interpolated value of the quantity q becomes [25, 26]

$$q_p = \sum_i q_i \Lambda\left(\frac{x_i - x_p}{\delta x}\right). \quad (13)$$

Similarly, one can revert the same procedure to get the values of the field q at mesh points

$$q_i = \sum_p q_p \Lambda\left(\frac{x_p - x_i}{\delta x}\right). \quad (14)$$

To conserve the first r moments, the interpolation kernel must satisfy the following condition

$$\sum_i q_i (x_i - x)^\alpha = \sum_p q_p (x_p - x)^\alpha, \quad (15)$$

where $0 \leq \alpha < r$. It is clear that $r = 0$ implies the conservation of the field q . The first r moments of the field q_i can be obtained using Eq. (13),

$$\sum_i q_i (x_i - x)^\alpha = \sum_p q_p \sum_i \Lambda \left(\frac{x_p - x_i}{\delta x} \right) (x_i - x)^\alpha. \quad (16)$$

Using the Newton formula, one can write the latter as

$$\begin{aligned} \sum_i q_i (x_i - x)^\alpha &= \\ \sum_p q_p \sum_{k=0}^{\alpha} \sum_i \Lambda \left(\frac{x_p - x_i}{\delta x} \right) x_i^k (-x)^{\alpha-k} \binom{\alpha}{k}. \end{aligned} \quad (17)$$

Finally, we note that the latter formula can be reduced to

$$\begin{aligned} \sum_i q_i (x_i - x)^\alpha &= \sum_p q_p \sum_{k=0}^{\alpha} x_p^k (-x)^{\alpha-k} \binom{\alpha}{k} \\ &= \sum_p q_p (x_p - x)^\alpha, \end{aligned} \quad (18)$$

if and only if

$$\sum_i \Lambda \left(\frac{x_p - x_i}{\delta x} \right) x_i^k = x_p^k. \quad (19)$$

In other words, the property (19) is the necessary condition for the interpolation kernel Λ to conserve the first r moments, i.e. to satisfy Eq. (15). However, it can be shown that applying condition (19) on a 4-point stencil leads to the Everett's formula (12).

3.1.3. B-Splines

It is well-known that interpolation schemes may introduce large errors when large fluctuations are present [26]. For this purpose, B-Splines are designed such that these effects are minimized [23]. B-Splines are non-negative

functions that are generated recursively by

$$B^{n+1}(x) = B^n(x) * B^0(x), \quad (20)$$

where $*$ is the convolution operator and

$$B^0(x) = \begin{cases} 1, & |x| \leq 1/2, \\ 0, & \text{otherwise,} \end{cases} \quad (21)$$

is the nearest grid point (NGP) interpolation. The first two members of the B-Spline family fall into the category of ordinary interpolation functions, meaning $B^n(0) = 1; n < 2$, while the rest are smoothing functions since $B^n(0) \neq 1; n \geq 2$.

B-Spline kernels are smooth functions and they have an accuracy of $\mathcal{O}(\delta x^2)$. In ref. [24], it was shown that their order of accuracy can be improved for $n \geq 2$ using Richardson extrapolation. The resulting function is,

$$K_n = \frac{1}{2} \left[3B_n - h \frac{\partial B_n}{\partial h} \right], \quad (22)$$

where $h = \delta x$ is the grid spacing and the derivative of B is not defined everywhere for $n < 2$. Finally, reminding the notation of u , the third-order accurate improved B-Spline is derived as,

$$K_3(u) = \begin{cases} 1 - \frac{5}{2}u^2 - \frac{3}{2}u^3, & 0 \leq u \leq 1, \\ \frac{1}{2}(2-u)^2(1-u), & 1 \leq u \leq 2, \\ 0, & \text{otherwise.} \end{cases} \quad (23)$$

Both L_4 and K_3 kernels are depicted in Fig. 2. One could observe that the K_3 kernel is much smoother than its counterpart and has a continuous derivative through its defined range. Also, it is visible that both kernels possess negative values which is known to cause oscillatory solutions in sharp contacts. We will address this issue in the followings.

3.2. High-resolution shock-capturing schemes

As a classic issue in computational fluid dynamics, the central high-order discretized schemes introduce high-frequency oscillations at the location of shocks and discontinuities. While the amplitude of these oscillations depends on the strength of the shock among other factors, they seem to persist despite

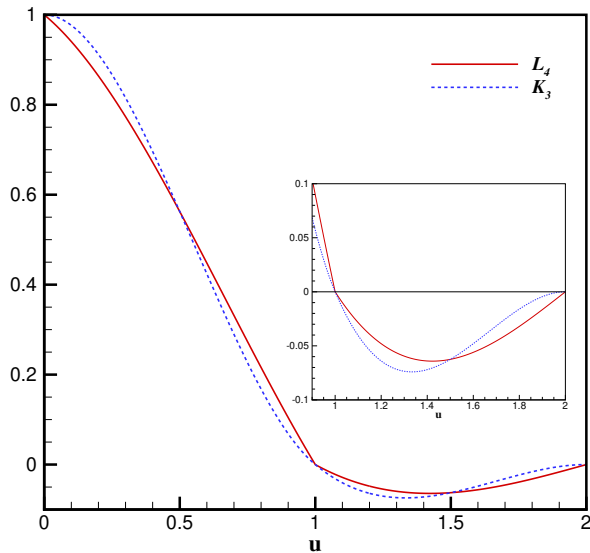


Figure 2: Comparison between L_4 and K_3 kernels. Contrary to L_4 , K_3 is smooth and its derivative is defined everywhere (See inset).

the size of the grid. This anomaly which is known as the Gibbs phenomena, can render the numerical scheme unacceptable. Different approaches have been developed to tackle this challenge. Among those, two fundamental methods have long and successfully been used in shock-capturing simulations: ENO and its successors such as WENO or TENO and TVD limiters [1]. Both schemes are robust in terms of capturing the discontinuities without spurious solutions, however the TVD schemes in general are known to be more dissipative [27].

In this work, we will make use of both methods for the following purposes: first, as any other numerical scheme, to be able to have accurate solutions in compressible shock-including simulation. Second, the PonD method depends on the square root of local temperature at its core (see Eq. (1)). Hence any oscillation that can push the temperature to negative values can not be allowed. This is particularly concerning in high Mach flows [28].

3.2.1. WENO interpolation

While the main idea of WENO is based on choosing the smoothest kernel when interpolating at cell interfaces [29], here we deal with an interpolation problem at arbitrary points in space. However, one can use the very same concept in designing an oscillation-free interpolation function. To construct

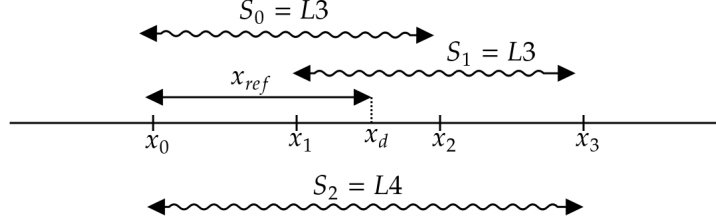


Figure 3: Schematics of the fourth order WENO interpolation in one dimension.

a fourth-order interpolation scheme augmented with the essence of WENO, we consider a central 4-point kernel around the departure point. Figure 3 illustrates a one-dimensional schematic of such setup. The main stencil is divided into two smaller stencils, i.e. $S_2 = S_1 \cup S_2$, where Lagrange polynomials are used in each of the stencils. The corresponding ideal weights of the sub-stencils are obtained as

$$\gamma_0 = 1 - \frac{x_{ref}}{3\delta x}, \quad (24)$$

$$\gamma_1 = \frac{x_{ref}}{3\delta x}, \quad (25)$$

where $x_{ref} = x_d - x_0$ and x_d is the departure point. If we are interested in interpolating the function $u(x)$, the final value of the interpolated function at the departure point becomes

$$u(x_d) = \sum_{k=0}^{k=1} w_k u^{(k)}, \quad (26)$$

where

$$w_k = \frac{\tilde{w}_k}{\sum_k \tilde{w}_k} \quad (27)$$

is the normalized weights, $u^{(k)}$ is the interpolated value in each sub-stencil and

$$\tilde{w}_k = \frac{\gamma_k}{(\epsilon + \beta_k)^2}. \quad (28)$$

The parameter ϵ is chosen as 10^{-6} to avoid zero denominator and β_k is the smoothness indicator of each stencil defined as [30]

$$\beta_k = \sum_{l=1}^2 \int_{x_1}^{x_2} \frac{d^l}{dx^l} u^{(k)}(x), \quad (29)$$

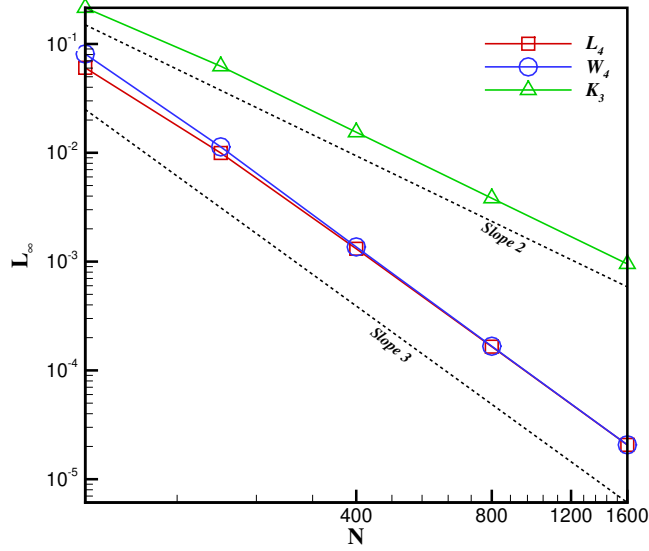


Figure 4: OVS of L_4 , K_3 and W_4 interpolation schemes. The results are obtained by solving the advection equation at $CFL = 0.1$.

where they are obtained as

$$\beta_0 = \frac{1}{12} (13u_0^2 - 52u_0u_1 + 26u_0u_2 + 64u_1^2 - 76u_1u_2 + 25u_2^2), \quad (30)$$

$$\beta_1 = \frac{1}{12} (25u_1^2 - 76u_1u_2 + 26u_1u_3 + 64u_2^2 - 52u_2u_3 + 13u_3^2). \quad (31)$$

Figure (4) shows the results of the order verification study (OVS) of the current scheme entitled as W_4 together with the L_4 and K_3 interpolation kernels. The results are the outcome of the semi-Lagrangian solution of the advection equation initialized with a Gaussian profile. The CFL number is fixed at 0.1. As expected, the underlying order of accuracy of all schemes are recovered.

3.2.2. TVD Bspline limiters

The so-called TVD scheme introduced by Harten, has been an effective tool in the class of high-resolution schemes to control the spurious oscillations

[27]. By definition, the total variation of a solution at time n is

$$TV[n] = \sum_i |u_{i+1}^n - u_i^n| \quad (32)$$

and a numerical scheme is said to be TVD if $TV[n+1] \leq TV[n]$ [31]. Based on this definition, the so-called limiter functions are designed to retain the smoothness of the solutions at critical points. More detailed information on limiters can be found in various researchs, such as [31, 32, 27].

As discussed in section 3.1.3, Bsplines are smooth functions and have better performance in interpolating fields with fluctuations than their counterparts due to their continuous derivatives [26]. In our numerical experiments, we also observe the very good mass conserving property of the K_3 kernel than L_4 and W_4 . However, they still allow oscillations in discontinuous parts of the solution since negative weights are present (see Fig. 2). Hence, to benefit from the mass-conserving feature of the K_3 kernel in high Mach compressible simulations, we aim at developing a TVD limiter function based on this kernel.

According to Eq. (23), on a symmetric 4-point stencil, K_3 has the following weights around the interpolation point (see Fig. 5)

$$\begin{aligned} a_{i-2} &= -\frac{1}{2}x_{ref}(1-x_{ref})^2, \\ a_{i-1} &= -\frac{3}{2}(1-x_{ref})(x_{ref}-x_1)(x_{ref}-x_2), \\ a_i &= -\frac{3}{2}(x_{ref})(1-x_{ref}-x_1)(1-x_{ref}-x_2), \\ a_{i+1} &= -\frac{1}{2}(1-x_{ref})x_{ref}^2, \end{aligned} \quad (33)$$

where $x_{1,2} = (1 \pm \sqrt{7})/3$ and $x_{ref} = x_d - x_{i-1}$. The weights (33) are realized on a grid with $\delta x = 1$ and they sum to one. We can generalize this interpolation scheme to a semi-Lagrangian advection problem with the CFL number defined as $\sigma = v\delta t/\delta x$, where v is a characteristic velocity and δt is the timestep. If we assume that $|\sigma| < 1$, then x_d in Fig. 5 is the departure point found by traveling back in time from the monitoring point x_i through the characteristic velocity $v > 0$. where the weights a_j are given by Eq. (33).

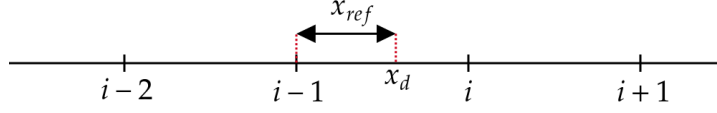


Figure 5: Support points of the K_3 kernel around the interpolation point.
In other words, we can rewrite the advection problem as

$$u_i^{n+1} = \sum_{j=i-2}^{i+1} a_j u_j^n, \quad (34)$$

However, it is logical to recast the weights as a function of the CFL number and independent of the grid size. By doing so, we derive

$$\begin{aligned} a_{i-2} &= -\frac{1}{2}\sigma^2(1-\sigma), \\ a_{i-1} &= -\frac{1}{2}\sigma(3\sigma^2 - 4\sigma - 1), \\ a_i &= -\frac{1}{2}(1-\sigma)(3\sigma^2 - 2\sigma - 2), \\ a_{i+1} &= -\frac{1}{2}\sigma(1-\sigma)^2, \end{aligned} \quad (35)$$

where $\sum_j a_j = 1$ and $\sigma > 0$. Finally the advection problem with a K_3 interpolation scheme can be rewritten as

$$\begin{aligned} u_i^{n+1} &= u_i^n - \sigma \delta u_{i-1/2}^n - \frac{\sigma}{2}(1-\sigma)^2 \delta u_{i+1/2}^n \\ &\quad + \frac{\sigma}{2}(1-\sigma)(1-2\sigma) \delta u_{i-1/2}^n + \frac{\sigma^2}{2}(1-\sigma) \delta u_{i-3/2}^n, \end{aligned} \quad (36)$$

where $\delta u_{i\pm k/2} = u_{i\pm k/2+1/2} - u_{i\pm k/2-1/2}$ is the central difference operator. We now proceed with the imposing the TVD limiter functions on the above equation

$$\begin{aligned} u_i^{n+1} &= u_i^n - \sigma \delta u_{i-1/2}^n - \frac{\sigma}{2}(1-\sigma)^2 \delta u_{i+1/2}^n \Phi_{i+1/2} \\ &\quad + \frac{\sigma}{2}(1-\sigma)(1-2\sigma) \delta u_{i-1/2}^n \Phi_{i-1/2} \\ &\quad + \frac{\sigma^2}{2}(1-\sigma) \delta u_{i-3/2}^n \Phi_{i-3/2}. \end{aligned} \quad (37)$$

To relate the limiters to the oscillations in the solution, they are commonly defined as a function of slope ratios

$$\Phi_{i+1/2} = \Phi(r_{i+1/2}^+), \quad (38)$$

where the superscript denotes the positive CFL number and

$$r_{i+1/2}^+ = \frac{\delta u_{i-1/2}}{\delta u_{i+1/2}} = \frac{u_i - u_{i-1}}{u_{i+1} - u_i}, \quad (39)$$

is an example of slope ratios which in general is defined as the upwind difference divided by the central difference [27]. One can write the following

$$\Phi_{i+1/2} \delta u_{i+1/2} = \Phi_{i+1/2} \frac{\delta u_{i+1/2}}{\delta u_{i-1/2}} \delta u_{i-1/2} = \frac{\Phi(r_{i+1/2}^+)}{r_{i+1/2}^+} \delta u_{i-1/2}, \quad (40)$$

$$\Phi_{i-3/2} \delta u_{i-3/2} = \Phi_{i-3/2} \frac{\delta u_{i-3/2}}{\delta u_{i-1/2}} \delta u_{i-1/2} = \frac{\Phi(r_{i-3/2}^-)}{r_{i-3/2}^-} \delta u_{i-1/2}. \quad (41)$$

To keep consistency, we rewrite the latter as

$$\frac{\Phi(r_{i-3/2}^-)}{r_{i-3/2}^-} \delta u_{i-1/2} = \Phi\left(\frac{1}{r_{i-1/2}^+}\right) r_{i-1/2}^+ \delta u_{i-1/2}. \quad (42)$$

Adopting the notations $r = r_{i+1/2}^+$ and $s = r_{i-1/2}^+$, we can rewrite Eq. (37) in the following compact form

$$u_i^{n+1} = u_i^n - \delta u_{i-1/2}^n \times \sigma \left(1 + \frac{1}{2}(1 - \sigma) \left[(1 - \sigma) \frac{\Phi(r)}{r} + (2\sigma - 1)\Phi(s) - \sigma s \Phi\left(\frac{1}{s}\right) \right] \right). \quad (43)$$

Finally, repeating the same procedure for the negative CFL number, the necessary condition for the scheme to be TVD is found as

$$-\frac{2}{1 - |\sigma|} \leq (1 - |\sigma|) \frac{\Phi(r)}{r} + (2|\sigma| - 1)\Phi(s) - |\sigma|s \Phi\left(\frac{1}{s}\right) \leq \frac{2}{|\sigma|}. \quad (44)$$

To find the suitable range of the limiter function, the following conditions are considered

$$\begin{aligned} \Phi(r) &= 0, \text{ if } r \leq 0, \\ \Phi(r) &> 0, \text{ if } r > 0, \\ \Phi(r) &= 1, \text{ if } r = 1. \end{aligned} \quad (45)$$

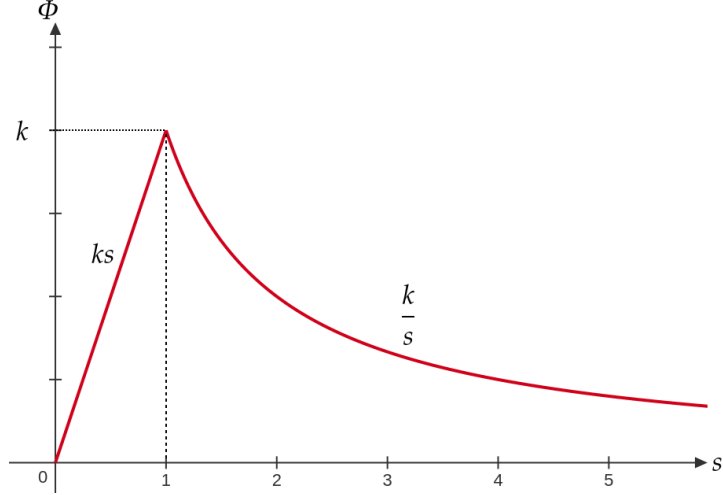


Figure 6: Asymptotic form of the limiter function. For any point s , $\Phi(1/s) = \Phi(s)$.

Two distinct steps are considered. First we assume $r > 0, s < 0$. Considering the constraints (45), Eq. (44) becomes

$$\Phi(r) \leq \frac{2r}{|\sigma|(1-|\sigma|)}, \quad (46)$$

where the most stringent condition gives

$$\Phi(r) \leq 8r. \quad (47)$$

In the second step, we assume the opposite as before, i.e. $r < 0, s > 0$ which renders Eq. (44) as

$$-\frac{2}{1-|\sigma|} \leq (2|\sigma|-1)\Phi(s) - |\sigma|s\Phi\left(\frac{1}{s}\right) \leq \frac{2}{|\sigma|}. \quad (48)$$

To have a sensible evaluation of the function $\Phi(1/s)$, we assume that the limiter function has the form $\Phi(s) = \min(ks, k/s)$ as shown in Fig. 6. This form of definition implies $\Phi(1/s) = \Phi(s)$. Hence, we can write the above equation as

$$-\frac{2}{1-|\sigma|} \leq ((2|\sigma|-1) - s|\sigma|)\Phi(s) \leq \frac{2}{|\sigma|}. \quad (49)$$

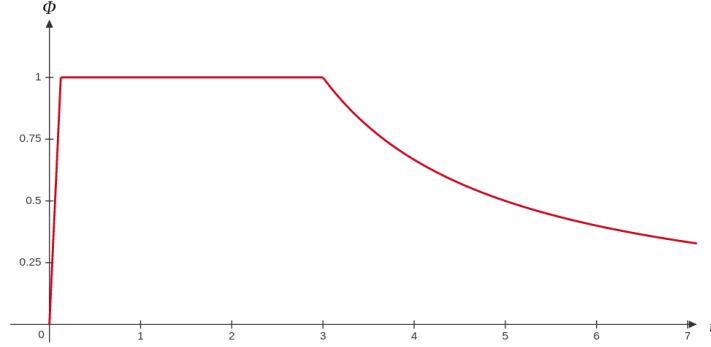


Figure 7: The K_3 limiter function

The following restraints can be derived

$$\begin{aligned} \Phi(s) &\leq \frac{2}{(1 - |\sigma|)(s|\sigma| - 2|\sigma| + 1)}, \quad |\sigma| < 0.5, \\ \Phi(s) &\leq \frac{2}{\eta |s|\sigma| - 2|\sigma| + 1|}, \quad |\sigma| > 0.5, \end{aligned} \quad (50)$$

where

$$\eta = \begin{cases} |\sigma|, & 0 < s < \frac{2|\sigma|-1}{|\sigma|}, \\ 1 - |\sigma|, & s > \frac{2|\sigma|-1}{|\sigma|}. \end{cases} \quad (51)$$

Finally, collecting the conditions (47) and (50), the most stringent limiter is obtained as

$$\Phi(r) = \max \left[0, \min \left(8r, 1, \frac{2}{r-1} \right) \right], \quad (52)$$

which is illustrated in Fig. 7.

To put the developed schemes into test, we solve the linear advection equation

$$\begin{aligned} u_t + au_x &= 0, \quad 0 \leq x \leq 1, \\ u(x, 0) &= \begin{cases} 1, & 3/8 \leq x \leq 5/8, \\ 0, & \text{otherwise,} \end{cases} \end{aligned} \quad (53)$$

where a is the constant speed. We compute the solution up to $t = 2$ which amounts to two total periods. A semi-Lagrangian scheme is adopted. 200

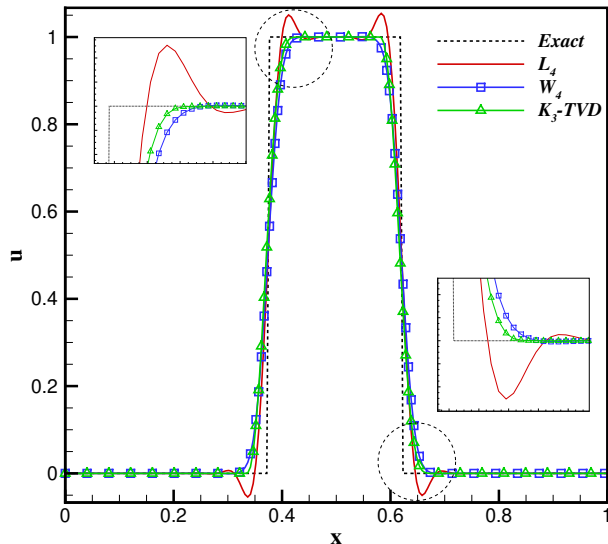


Figure 8: Semi-Lagrangian solution of the advection equation with L_4 , W_4 and $K_3 - TVD$ schemes after two periods.

points are used to discretize the space and the CFL number is $\sigma = a\delta t/\delta x = 0.4$. Figure 8 shows the results for the L_4 , W_4 and $K_3 - TVD$ schemes after two periods. As we can see, the oscillations at the discontinuities are successfully eliminated using the TVD and WENO schemes. .

4. Spectral Analysis

Since the present model is based on semi-Lagrangian advection, first we discuss the spectral properties of a linear interpolation scheme such as the dissipation and dispersion errors against the reduced wave number ζ in the interval $[0, \pi]$. Considering the field $u(x, t)$ that is advected by a constant velocity a and assuming a general discrete form $u_i(t) = \hat{u}(t) \exp(i\zeta x)$, the solution via the semi-Lagrangian advection in the time-interval of $[0, t]$ is obtained as

$$u_i(t) = \hat{u}(0) e^{i\zeta x} \sum_{j=-l}^r w_j e^{ij\zeta}, \quad (54)$$

where $w = w(\sigma)$ is the interpolation weights and $\sigma = at/\delta x$ is the CFL number. Finally, the modified wave number is derived with the following real and imaginary parts

$$\begin{aligned}\Re(\Psi) &= \frac{1}{\sigma} \ln R, \\ \Im(\Psi) &= -\frac{\theta}{\sigma},\end{aligned}\tag{55}$$

where (R, θ) are the modulus and argument of the complex term $\sum w_j \exp(ij\zeta)$, respectively. With this, one can write the discrete solution as [33]

$$u_i(t) = \hat{u}(0)e^{i\zeta}e^{-i\sigma\Psi},\tag{56}$$

where spectral schemes feature $\Psi(\zeta) = \zeta$.

While this theory can be employed for analysis of the dissipation and dispersion errors of linear models, the spectral properties of nonlinear schemes such as the shock-capturing methods are derived using the approximate dispersion relation (ADR) proposed by Pirozzoli [33]. Assuming a sinusoidal initial condition with different reduced wave numbers, we apply the ADR method to the WENO and $K_3 - \text{TVD}$ schemes. Figure 9 shows the spectral properties of both schemes along with the dispersion and dissipation of the linear L_4 and K_3 functions. As we see, the results from the ADR analysis coincide with those obtained from theory (Eq. (55)) for the linear schemes. It is also observed that while the L_4 scheme has a superior dispersion property, the K_3 scheme features much less dissipation almost as the spectral. Regarding the non-linear schemes, the $K_3 - \text{TVD}$ has an improved dispersion property and follows the spectral closely up to the reduced wave number $\zeta = \pi/2$, while becoming more dissipative. On the other hand, the wave-resolution property of the WENO-interpolation scheme follows the spectral up to $\zeta = 1.2$, i.e. low to moderate wave numbers. Finally, all schemes are stable through the entire range of wave numbers, where $\text{Im}(\Psi) \leq 0$.

5. Benchmarks

In this section, we will use W_4 and $K_3 - \text{TVD}$ schemes in the PonD framework. To verify the accuracy and robustness, a various number of standard compressible benchmarks are considered. In each test case, we will assess the performance of both lattice geometries. In the following, we will

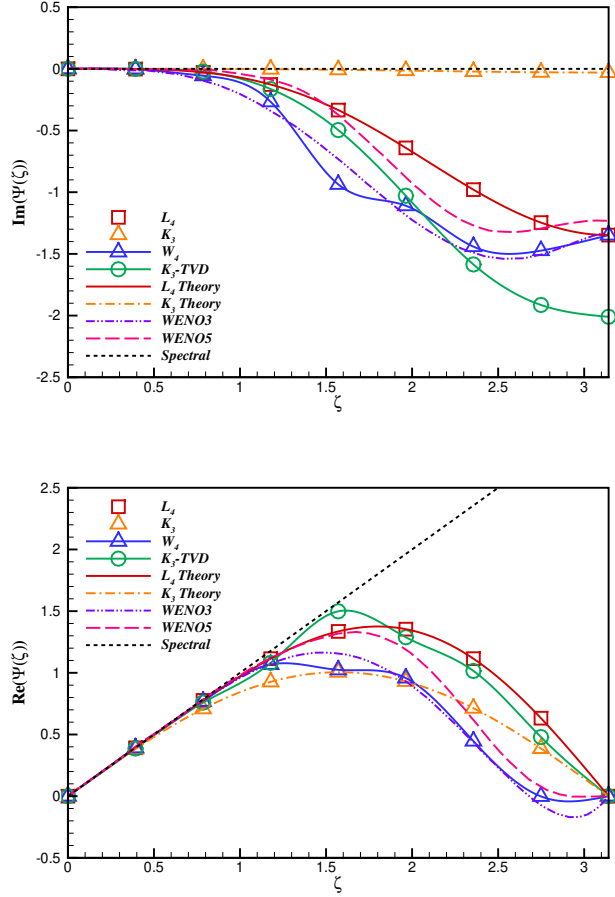


Figure 9: Approximate dispersion relation for various linear and shock-capturing schemes: dissipation (top) and dispersion (bottom).

first consider the two most common mild shock-tube problems, the Sod and the Lax shock-tube. Then the simulation of the Shu-Osher problem as a rather stronger case will be presented followed by considering some strong cases. In our TVD scheme, we choose the zeroth moment of each set of populations as the slope ratio determinant for the corresponding population, i.e. density for the f population and total energy for the g , unless stated otherwise. The CFL number in our simulations are based on the maximum magnitude of the discrete velocities

$$\text{CFL} = \frac{\max(\|\mathbf{v}_i\|)\delta t}{\delta x} \quad (57)$$

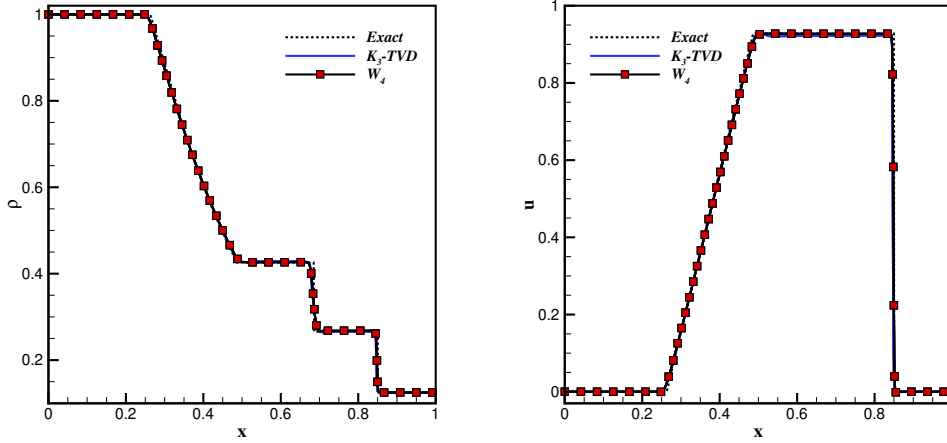


Figure 10: Sod shock-tube problem: density distribution (left) and velocity distribution (right). "Exact" represents the solution of the Riemann problem. $Nx = 600$ points are used to discretize the domain.

and is fixed to $CFL = 0.2$. The viscosity is chosen small enough such that the simulations are stable ($\nu\delta t/\delta x^2 \approx \mathcal{O}(10^{-6} - 10^{-4})$). We use the standard $D2Q9$ lattice in all simulations.

5.1. Sod problem

The initial condition for the Sod problem is [34]:

$$(\rho, u, p) = \begin{cases} (1, 0, 1) & \text{if } 0 \leq x < 0.5, \\ (0.125, 0, 0.1) & \text{if } 0.5 \leq x \leq 1, \end{cases} \quad (58)$$

where x is the non-dimensional length of the tube and the final simulation time is $t = 0.2$. $Nx = 600$ points are used to discretize the domain. Figure 10 shows the results for the density and velocity distributions using the $K_3 - TVD$ and W_4 schemes. Both schemes have similar performances, where the results agree well with the exact solution. It is also visible that both schemes have successfully captured the shock and the discontinuity free of oscillations.

5.2. Lax problem

We consider the Lax problem [35] with the initial condition of

$$(\rho, u, p) = \begin{cases} (0.445, 0.689, 3.528) & \text{if } 0 \leq x < 0.5, \\ (0.5, 0, 0.571) & \text{if } 0.5 \leq x \leq 1. \end{cases} \quad (59)$$

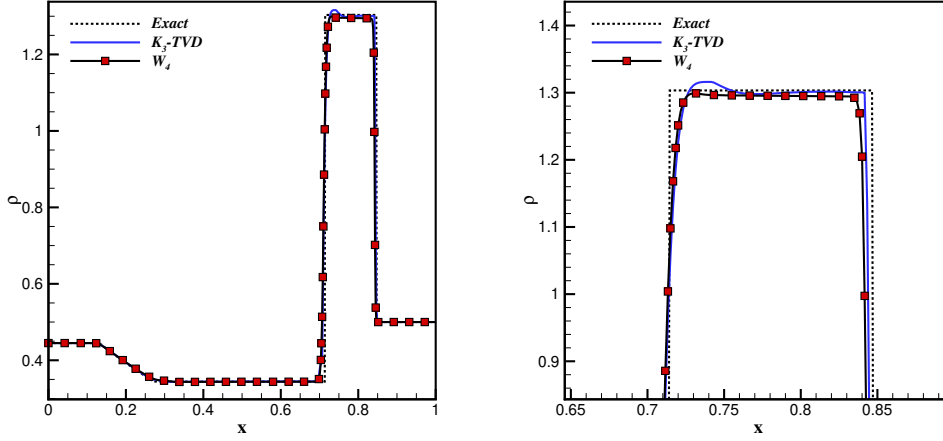


Figure 11: Lax shock-tube problem: density distribution for K_3 – TVD and W_4 schemes (left) and a zoom of the density distribution around the peak values (right). "Exact" represents the solution of the Riemann problem. $Nx = 600$ points are used to discretize the domain.

The final simulation time is $t = 0.14$. The domain is discretized using $Nx = 600$ points. Figure 11 shows the results for the density distribution. As we can observe, the monotonicity of the solution is well preserved near the contact discontinuity and the shock-wave in both schemes. Furthermore, the results are in good agreement with the exact solution.

5.3. Shock density-wave interaction

Also known as the Shu-Osher problem [36], a Mach 3 shock wave interacts with a perturbed density field leading to discontinuities and small structures. The initial condition for this problem is

$$(\rho, u, p) = \begin{cases} (3.857, 2.629, 10.333) & \text{if } 0 \leq x < 1, \\ (1 + 0.2 \sin(5x), 0, 1) & \text{if } 1 \leq x \leq 10. \end{cases} \quad (60)$$

The final simulation time is $t = 1.8$. $Nx = 800$ points are used for discretizing the space. Figure 12 shows the results for the density distribution compared to the exact solution. We observe that the WENO scheme acts inferior in this simulation. As seen in Fig. 13, the acoustic waves are overestimated and they show a convergent behavior, i.e. they do not improve by increasing the resolution. On the other hand, the TVD scheme captures the proper amplitude of the acoustic waves and the entropy waves are better resolved

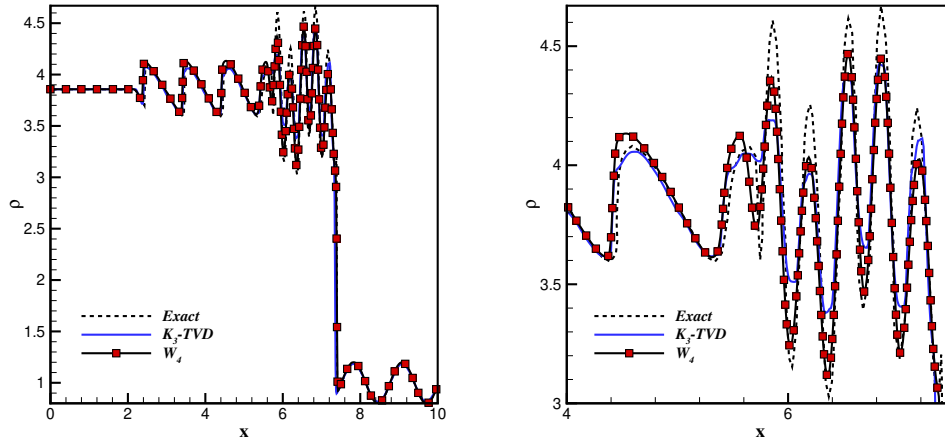


Figure 12: Shu-Osher problem using the K_3 – TVD and W_4 schemes: density distribution (left) and a zoom of the density distribution (right). $Nx = 800$ points are used.

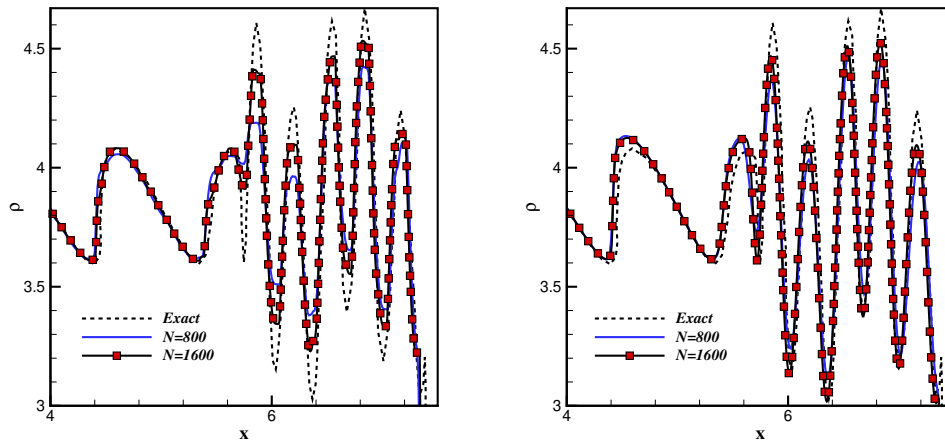


Figure 13: Shu-Osher problem: A zoom of the density distribution using the K_3 – TVD scheme(left) and W_4 scheme (right) at different resolutions.

with increasing the resolution. Nevertheless, the shock is captured free of oscillations in both schemes.

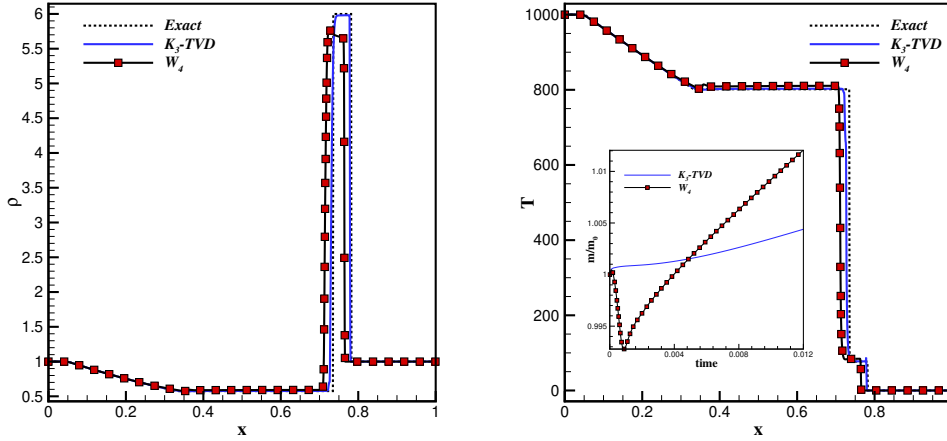


Figure 14: Strong shock-tube problem: density distribution (left) and temperature profile (right) using the K_3 – TVD and W_4 schemes with $Nx = 1600$ grid points. "Exact" represents the solution of the Riemann problem. The inset at the right picture shows the dimensionless mass of the domain for both schemes throughout the simulation.

5.4. Strong shock-tube

We consider a strong shock-tube case where the value of the Mach number reaches to 198 [37]. The initial conditions are

$$(\rho, u, p) = \begin{cases} (1, 0, 1000) & \text{if } 0 \leq x < 0.5, \\ (1, 0, 0.01) & \text{if } 0.5 \leq x \leq 1, \end{cases} \quad (61)$$

where the temperature ratio of both sides is 10^5 . The final simulation time is $t = 0.012$. Figure 14 shows a comparison of the computed density field against the exact solution, using $Nx = 1600$ grid points. As we can notice, the location of the shock and the contact discontinuity is captured free of oscillations by both schemes, while the WENO scheme does not coincide with the exact solution. This is visible in both density and temperature profiles. This could be explained by looking at the evolution of total mass of the domain throughout the simulation. The TVD scheme features a very well mass conservation than that of the WENO (see inset). Eventually, the mass change in the WENO scheme leads to deviations in capturing the correct location of the shock front.

5.5. Le Blanc Problem

Known as an extreme test case with very strong discontinuities, the Le Blanc problem [38] has the following initial conditions

$$(\rho, u, p) = \begin{cases} (1, 0, 2/3 \times 10^{-1}) & \text{if } 0 \leq x < 3, \\ (10^{-3}, 0, 2/3 \times 10^{-10}) & \text{if } 3 \leq x \leq 9. \end{cases} \quad (62)$$

The final simulation time is $t = 6$ and $Nx = 4000$ grid points are used. The adiabatic coefficient is set to $\gamma = 5/3$. Figure 15 shows the results for the density, pressure and velocity distribution using the K_3 -TVD scheme, where they agree well with the reference solutions. The WENO scheme failed this simulation.

5.6. Double Mach Reflection

The initial condition for this case is [39]

$$(\rho, u, v, p) = \begin{cases} (1.4, 0, 0, 1), & \text{if } y > 1.732(x - 0.1667), \\ (8, 7.145, -4.125, 116.8333), & \text{otherwise,} \end{cases} \quad (63)$$

which describes a right-moving Mach 10 incident shock wave initially placed at $x=0.1667$, with an incidence angle of 60° to the x -axis. The computational domain is $[0,4] \times [0,1]$ and the final simulation time is $t = 0.2$. The post-shock condition is applied to the left boundary, whereas zero-gradient of all fluid variables is applied to the right boundary. At the bottom boundary, the post-shock condition is imposed from $x = 0$ to $x = 0.1667$, while a reflecting wall condition is enforced from $x = 0.1667$ to $x = 4$. The top boundary is treated such that all the fluid variables follow the evolution of the traveling shock-wave. For this simulation, we choose $Nx \times Ny = 1201 \times 301$ grid points. Figure 16 shows the results for both K_3 -TVD and W_4 schemes compared to the reference solution [5], where temperature is used as the slope ratio determinant for the TVD scheme. To facilitate the comparison, only a part of the domain is presented. We observe that with the TVD scheme, the flow features and their locations are in good match with the reference solution. On the other hand, a close assessment of the results corresponding to the WENO scheme reveals some discrepancies with respect to the reference solution, such as the location of the second triple point. However, less dissipation than the TVD scheme is apparent in the jet area, where more

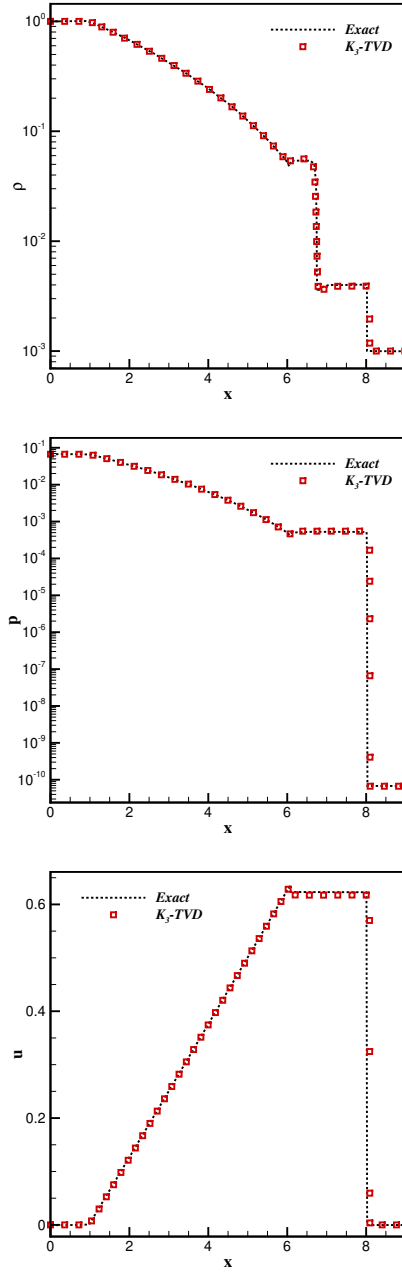


Figure 15: Le Blanc problem: from top to bottom; density, pressure and velocity distribution using the K_3 TVD scheme. $Nx = 4000$ points are used.

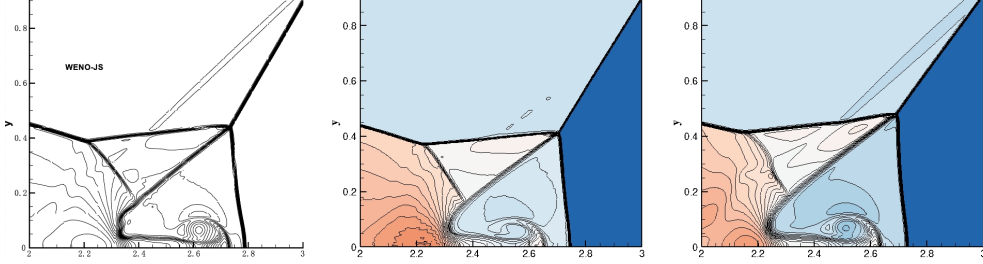


Figure 16: Double Mach reflection of a strong shock: density contours in reference solution using WENO-JS-5 [5] (left), present model using the K_3 -TVD scheme (middle) and the W_4 scheme (right). 43 contours are drawn between 1.887 and 20.9. Reference figures reprinted from [5] with permission from Elsevier.

flow structures are resolved. Overall, the comparison of density contour lines suggests that the TVD scheme is more accurate in this simulation.

5.7. Astrophysical jet

Astrophysical jets refer to high-speed gas flows with extremely high Mach numbers that are captured by the Hubble Space Telescope. In this section, we consider a two-dimensional astrophysical jet without radioactive cooling [40]. From the computational point of view, this is a very challenging case since the extremely high kinetic energy may lead to negative internal energy. The computational domain is $[0, 2] \times [-0.5, 0.5]$. The initial conditions are

$$(\rho, u, v, p) \tag{64}$$

$$= \begin{cases} (5, 11, 0, 0.4127) & \text{if } x = 0 \text{ and } -0.05 \leq y \leq 0.05, \\ (0.5, 0, 0.4127) & \text{otherwise,} \end{cases} \tag{65}$$

which leads to Mach 30 with respect to the cold jet. The computed density and pressure contours are illustrated in Fig. 17 using the TVD scheme (temperature used as the determinant), where the bow shock is visible propagating into the ambient medium. It can be noticed that the instabilities that appear around the jet are captured. It is expected that augmenting the model with a positivity preserving limiter would lead to stable simulations for higher Mach numbers [40, 28, 41, 42]. It must be commented that the WENO scheme failed this simulation.

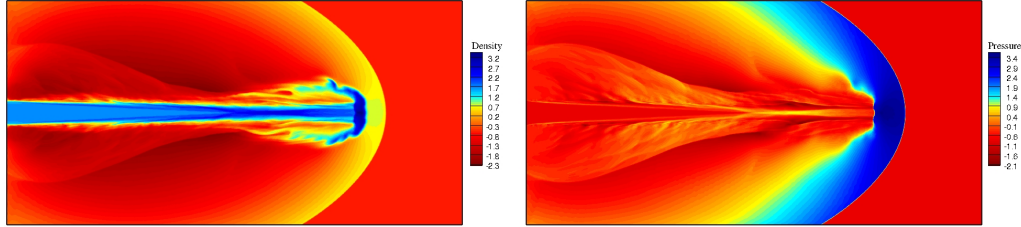


Figure 17: Astrophysical jet problem: density (left) contours and pressure (right) contours of logarithmic scale using the $K_3 - \text{TVD}$ scheme with 1000×500 grid points.

6. Conclusion

In this paper, we presented simulations of compressible flows in the PonD framework. Using the shock capturing schemes such as WENO and TVD, we were able to implement simulations in a wide range of Mach numbers; from mild cases such as sod shock-tube to astrophysical jets. Comparison between the two numerical schemes were presented at each benchmark.

The results show that the PonD model is able to handle highly supersonic flows when augmented with proper numerical schemes. Moreover, it was observed that the TVD scheme features better performance in terms of accuracy and mass conservation. However, for extreme cases, the model must be equipped with more sophisticated techniques such as the positivity preserving schemes.

7. acknowledgments

This work was supported by the European Research Council (ERC) Advanced Grant No. 834763-PonD and the SNF Grant No. 200021-172640 (E.R.). Computational resources at the Swiss National Super Computing Center (CSCS) were provided under Grants No. s897 and No. s1066.

References

- [1] S. Pirozzoli, Numerical methods for high-speed flows, Annual review of fluid mechanics 43 (2011) 163–194.

- [2] A. Harten, High resolution schemes for hyperbolic conservation laws, *Journal of Computational Physics* 49 (3) (1983) 357–393. doi:[https://doi.org/10.1016/0021-9991\(83\)90136-5](https://doi.org/10.1016/0021-9991(83)90136-5). URL <https://www.sciencedirect.com/science/article/pii/S0021999183901365>
- [3] A. Harten, B. Engquist, S. Osher, S. R. Chakravarthy, Uniformly high order accurate essentially non-oscillatory schemes, III, *Journal of Computational Physics* 71 (2) (1987) 231–303. doi:[https://doi.org/10.1016/0021-9991\(87\)90031-3](https://doi.org/10.1016/0021-9991(87)90031-3). URL <https://www.sciencedirect.com/science/article/pii/S0021999187900313>
- [4] X.-D. Liu, S. Osher, T. Chan, Weighted Essentially Non-oscillatory Schemes, *Journal of Computational Physics* 115 (1) (1994) 200–212. doi:<https://doi.org/10.1006/jcph.1994.1187>. URL <https://www.sciencedirect.com/science/article/pii/S0021999184711879>
- [5] L. Fu, X. Y. Hu, N. A. Adams, A family of high-order targeted ENO schemes for compressible-fluid simulations, *Journal of Computational Physics* 305 (2016) 333–359. doi:<https://doi.org/10.1016/j.jcp.2015.10.037>. URL <https://www.sciencedirect.com/science/article/pii/S0021999115007147>
- [6] C. Kunert, J. Harting, Roughness induced boundary slip in microchannel flows, *Physical Review Letters* 99 (17) (2007) 176001. arXiv:0705.0270, doi:10.1103/PhysRevLett.99.176001. URL <https://link.aps.org/doi/10.1103/PhysRevLett.99.176001>
- [7] J. Hyväluoma, J. Harting, Slip flow over structured surfaces with entrapped Microbubbles, *Physical Review Letters* 100 (24) (2008) 246001. arXiv:0801.1448, doi:10.1103/PhysRevLett.100.246001. URL <https://link.aps.org/doi/10.1103/PhysRevLett.100.246001>
- [8] M. Sbragaglia, R. Benzi, L. Biferale, S. Succi, F. Toschi, Surface roughness-hydrophobicity coupling in microchannel and nanochannel flows, *Physical Review Letters* 97 (20) (2006) 204503. doi:10.1103/

PhysRevLett.97.204503.

URL <https://link.aps.org/doi/10.1103/PhysRevLett.97.204503>

- [9] L. Biferale, P. Perlekar, M. Sbragaglia, F. Toschi, Convection in multiphase fluid flows using lattice boltzmann methods, Physical Review Letters 108 (10) (2012) 104502. arXiv:1111.0905, doi:10.1103/PhysRevLett.108.104502.
URL <https://link.aps.org/doi/10.1103/PhysRevLett.108.104502>
- [10] R. Benzi, S. Chibbaro, S. Succi, Mesoscopic lattice Boltzmann modeling of flowing soft systems, Physical Review Letters 102 (2) (2009) 026002. doi:10.1103/PhysRevLett.102.026002.
URL <https://link.aps.org/doi/10.1103/PhysRevLett.102.026002>
- [11] A. Mazloomi M, S. S. Chikatamarla, I. V. Karlin, Entropic lattice Boltzmann method for multiphase flows, Physical Review Letters 114 (17) (2015) 174502. doi:10.1103/PhysRevLett.114.174502.
URL <https://link.aps.org/doi/10.1103/PhysRevLett.114.174502>
- [12] N. I. Prasianakis, I. V. Karlin, Lattice Boltzmann method for simulation of compressible flows on standard lattices, Physical Review E - Statistical, Nonlinear, and Soft Matter Physics 78 (1) (2008) 016704. doi:10.1103/PhysRevE.78.016704.
URL <https://journals.aps.org/pre/abstract/10.1103/PhysRevE.78.016704>
- [13] N. Frapolli, S. S. Chikatamarla, I. V. Karlin, Entropic lattice Boltzmann model for compressible flows, Physical Review E - Statistical, Nonlinear, and Soft Matter Physics 92 (6) (2015) 061301. doi:10.1103/PhysRevE.92.061301.
URL <https://journals.aps.org/pre/abstract/10.1103/PhysRevE.92.061301>
- [14] B. Dorschner, F. Bösch, I. V. Karlin, Particles on Demand for Kinetic Theory, Physical Review Letters 121 (13) (2018) 130602. arXiv:1806.05089, doi:10.1103/PhysRevLett.121.130602.

URL <https://journals.aps.org/prl/abstract/10.1103/PhysRevLett.121.130602>

- [15] D. Wilde, A. Krämer, D. Reith, H. Foysi, Semi-Lagrangian lattice Boltzmann method for compressible flows, *Physical Review E* 101 (5) (2020) 53306.
- [16] M. Atif, P. K. Kolluru, C. Thantapanally, S. Ansumali, Essentially entropic lattice boltzmann model, *Phys. Rev. Lett.* 119 (2017) 240602. doi:10.1103/PhysRevLett.119.240602.
URL <https://link.aps.org/doi/10.1103/PhysRevLett.119.240602>
- [17] B. Dorschner, F. Bösch, S. S. Chikatamarla, K. Boulouchos, I. V. Karlin, Entropic multi-relaxation time lattice boltzmann model for complex flows, *Journal of Fluid Mechanics* 801 (2016) 623–651.
- [18] S. Succi, *The lattice Boltzmann equation: for complex states of flowing matter*, Oxford University Press, 2018.
- [19] T. Krüger, H. Kusumaatmaja, A. Kuzmin, O. Shardt, G. Silva, E. M. Viggen, *The lattice boltzmann method*, Springer International Publishing 10 (978-3) (2017) 4–15.
- [20] S. S. Chikatamarla, I. V. Karlin, Lattices for the lattice boltzmann method, *Physical Review E* 79 (4) (2009) 046701.
- [21] I. V. Karlin, D. Sichau, S. S. Chikatamarla, Consistent two-population lattice Boltzmann model for thermal flows, *Physical Review E* 88 (6) (2013) 63310.
- [22] E. Reyhanian, B. Dorschner, I. V. Karlin, Thermokinetic lattice boltzmann model of nonideal fluids, *Physical Review E* 102 (2) (2020) 020103.
- [23] I. J. Schoenberg, Contributions to the problem of approximation of equidistant data by analytic functions, part a—on the problem of smoothing or gradation, a first class of analytic approximation formulae, *Quarterly of Applied Mathematics* 4 (1946) 45–99.
- [24] J. J. Monaghan, Extrapolating b splines for interpolation, *Journal of Computational Physics* 60 (2) (1985) 253–262.

- [25] W. M. van Rees, 3D simulations of vortex dynamics and biolocomotion, Ph.D. thesis, ETH Zurich (2014).
- [26] P. Koumoutsakos, Inviscid axisymmetrization of an elliptical vortex, *Journal of Computational Physics* 138 (2) (1997) 821–857.
- [27] M. Arora, P. L. Roe, A well-behaved TVD limiter for high-resolution calculations of unsteady flow, *Journal of Computational Physics* 132 (1) (1997) 3–11.
- [28] X. Zhang, C.-W. Shu, Positivity-preserving high order discontinuous Galerkin schemes for compressible Euler equations with source terms, *Journal of Computational Physics* 230 (4) (2011) 1238–1248.
- [29] G.-S. Jiang, C.-W. Shu, Efficient implementation of weighted ENO schemes, *Journal of computational physics* 126 (1) (1996) 202–228.
- [30] C.-W. Shu, Essentially non-oscillatory and weighted essentially non-oscillatory schemes, *Acta Numerica* 29 (2020) 701–762.
- [31] Y. N. Jeng, U. J. Payne, An adaptive TVD limiter, *Journal of Computational Physics* 118 (2) (1995) 229–241.
- [32] J. Shi, E. F. Toro, Fully discrete high-order shock-capturing numerical schemes, *International journal for numerical methods in fluids* 23 (3) (1996) 241–269.
- [33] S. Pirozzoli, On the spectral properties of shock-capturing schemes, *Journal of Computational Physics* 219 (2) (2006) 489–497.
- [34] G. A. Sod, A survey of several finite difference methods for systems of nonlinear hyperbolic conservation laws, *Journal of Computational Physics* 27 (1) (1978) 1–31. doi:[https://doi.org/10.1016/0021-9991\(78\)90023-2](https://doi.org/10.1016/0021-9991(78)90023-2).
URL <https://www.sciencedirect.com/science/article/pii/0021999178900232>
- [35] P. D. Lax, Weak solutions of nonlinear hyperbolic equations and their numerical computation, *Communications on pure and applied mathematics* 7 (1) (1954) 159–193.

- [36] C.-W. Shu, S. Osher, Efficient implementation of essentially non-oscillatory shock-capturing schemes, II, *Journal of Computational Physics* 83 (1) (1989) 32–78. doi:[https://doi.org/10.1016/0021-9991\(89\)90222-2](https://doi.org/10.1016/0021-9991(89)90222-2).
URL <https://www.sciencedirect.com/science/article/pii/S0021999189902222>
- [37] E. F. Toro, M. E. Vázquez-Cendón, Flux splitting schemes for the Euler equations, *Computers & Fluids* 70 (2012) 1–12.
- [38] R. Loubère, M. J. Shashkov, A subcell remapping method on staggered polygonal grids for arbitrary-lagrangian-eulerian methods, *Journal of Computational Physics* 209 (1) (2005) 105–138. doi:<https://doi.org/10.1016/j.jcp.2005.03.019>.
URL <https://www.sciencedirect.com/science/article/pii/S0021999105001841>
- [39] P. Woodward, P. Colella, The numerical simulation of two-dimensional fluid flow with strong shocks, *Journal of Computational Physics* 54 (1) (1984) 115–173. doi:[https://doi.org/10.1016/0021-9991\(84\)90142-6](https://doi.org/10.1016/0021-9991(84)90142-6).
URL <https://www.sciencedirect.com/science/article/pii/S0021999184901426>
- [40] X. Zhang, C.-W. Shu, On positivity-preserving high order discontinuous Galerkin schemes for compressible Euler equations on rectangular meshes, *Journal of Computational Physics* 229 (23) (2010) 8918–8934. doi:<https://doi.org/10.1016/j.jcp.2010.08.016>.
URL <https://www.sciencedirect.com/science/article/pii/S0021999110004535>
- [41] X. Zhang, C.-W. Shu, Positivity-preserving high order finite difference WENO schemes for compressible Euler equations, *Journal of Computational Physics* 231 (5) (2012) 2245–2258.
- [42] L. Fu, A very-high-order TENO scheme for all-speed gas dynamics and turbulence, *Computer Physics Communications* 244 (2019) 117–131.